UC Davis
UC Davis Previously Published Works

Title
Flagellar swimming in viscoelastic fluids: role of fluid elastic stress revealed by simulations based on experimental data

Permalink
https://escholarship.org/uc/item/6564692m

Journal
Journal of The Royal Society Interface, 14(135)

ISSN
1742-5689

Authors
Li, Chuanbin
Qin, Boyang
Gopinath, Arvind
et al.

Publication Date
2017-10-01

DOI
10.1098/rsif.2017.0289

Peer reviewed

Research

Flagellar swimming in viscoelastic fluids: role of fluid elastic stress revealed by simulations based on experimental data

Chuanbin Li[1], Boyang Qin[2], Arvind Gopinath[3], Paulo E. Arratia[2], Becca Thomases[1] and Robert D. Guy[1]

[1]Department of Mathematics, University of California Davis, Davis, CA 95616, USA
[2]Department of Mechanical Engineering and Applied Mechanics, The University of Pennsylvania, Philadelphia, PA 19104, USA
[3]Department of Bioengineering, University of California Merced, Merced, CA 95343, USA

RDG, 0000-0002-0602-7015

Many important biological functions depend on microorganisms' ability to move in viscoelastic fluids such as mucus and wet soil. The effects of fluid elasticity on motility remain poorly understood, partly because the swimmer strokes depend on the properties of the fluid medium, which obfuscates the mechanisms responsible for observed behavioural changes. In this study, we use experimental data on the gaits of *Chlamydomonas reinhardtii* swimming in Newtonian and viscoelastic fluids as inputs to numerical simulations that decouple the swimmer gait and fluid type in order to isolate the effect of fluid elasticity on swimming. In viscoelastic fluids, cells employing the Newtonian gait swim faster but generate larger stresses and use more power, and as a result the viscoelastic gait is more efficient. Furthermore, we show that fundamental principles of swimming based on viscous fluid theory miss important flow dynamics: fluid elasticity provides an elastic memory effect that increases both the forward and backward speeds, and (unlike purely viscous fluids) larger fluid stress accumulates around flagella moving tangent to the swimming direction, compared with the normal direction.

1. Introduction

Swimming microorganisms are important to many industrial and natural processes including the production of biofuels from algae, fermentation for vaccine and food production, and bio-mixing in oceans. Recently, there has been a resurgence of interest in the motility of microorganisms for technological applications that include micro- and nano-robotics [1–3], drug delivery [4,5] and cell manipulation [6,7]. While most of our current understanding of microorganism swimming is drawn from investigations in Newtonian fluids (e.g. water), many important biological processes occur in fluids that contain polymers and/or other solids, which introduce non-Newtonian properties to the fluid such as shear-thinning viscosity and elasticity. Examples include the swimming of flagellated sperm cells in cervical mucus during fertilization [8,9], motility of pathogens through tissues and stomach lining [10], and burrowing of worms in wet soil [11]. Importantly, the fluid rheological properties can significantly affect the motility kinematics of microorganisms [12–15].

Locomotion of microorganisms in viscoelastic fluids has received much recent attention due to its prevalence in biological processes [13,16–20]. Recent results highlight the challenges in understanding the effects of fluid elasticity on swimming. For example, simulations of two-dimensional finite-sized waving filaments [18,20] and rotating helices [21] suggest that fluid elasticity may *increase* propulsion speed. Similar trends are found in experiments with mechanically actuated rotating helices [22], magnetically driven physical models of undulatory swimmers [23], and *Escherichia coli* in polymeric solutions [14,24]. On the other hand, theoretical analysis of two-dimensional, infinitely long waving sheets

and filaments [13,17,25] as well as numerical simulations of idealized swimmers in viscoelastic fluids [19] show a *reduction* in propulsion speed compared with purely viscous fluids. These predictions are consistent with experiments with the undulating worm *Caenorhabditis elegans* [16] and with the green alga *Chlamydomonas reinhardtii* [15]. Moreover, these experiments show that fluid elasticity significantly modifies the organism's stroke kinematics such as the worm's swimming amplitude and the alga's flagellum beating frequency. The intricate relationship between fluid elasticity and swimming speed is difficult to understand from just experimental data because it is challenging to decouple fluid effects from the microorganism's swimming stroke kinematics.

In this paper, we investigate the effects of fluid elasticity and flagellar kinematics on the motility of the green alga *C. reinhardtii* using numerical simulations and experimental data. The eukaryotic biflagellated alga *C. reinhardtii* is a model organism found in soil and fresh water [26]. It is widely used in studies of ciliary kinematics and motility since its two flagella (approx. 10 μm in length) have the same conserved '9 + 2' microtubule arrangement seen in eukaryotic axonemes and respiratory cilia [27]. The algal cell swims using cyclical breast-stroke patterns with asymmetric power and recovery strokes [26,28], and generates far-field flows that have been recently characterized in experiments [29,30].

In [15], we investigated *C. reinhardtii* swimming and flagellar kinematics in fluids of different viscosity and elasticity, and we showed that the flagellar beat changed both shape and frequency in response to changes in fluid rheology. From our experimental data alone we cannot infer the mechanism behind the observed changes in swimming speed in response to fluid rheology because of the changes in gait. One way to address this difficulty is to perform numerical simulations of swimming *C. reinhardtii* using experimentally derived swimming gaits (or strokes), which can then be investigated in fluids of varying elasticity. Here, we focus on two particular strokes from [15] that have the same beating frequency, but one from a cell in a Newtonian fluid and the other from a cell in a viscoelastic fluid of the same viscosity. Thus, the only differences between these datasets are the elasticity of the fluid and the shape of the flagellar beat. We perform three-dimensional numerical simulations based on these two gaits, and we decouple the alga's flagellar gait from the fluid rheology by varying them independently in an effort to understand how fluid elasticity affects swimming.

We find that, as the organism swims in viscoelastic fluids, elastic stress accumulates at the distal tip of the flagella and the size of the elastic stress is larger during the return stroke than during the power stroke. These elastic stresses result in an elastic memory effect that propels the cell even when the flagella stop moving. This memory effect together with the larger accumulation of elastic stresses in the return stroke leads to a decrease in net forward speed, a trend observed in experiments [15]. We posit that the orientation of the flagella tips is the main contributor to the temporal asymmetry in accumulation of elastic stresses in the fluid, which is supported by simulations of a thin cylinder with different orientations moving in viscoelastic fluids. Surprisingly, we find that in viscoelastic fluids a cylinder moving along its axis generates larger fluid (elastic) stresses than a cylinder moving orthogonal to its axis; the opposite is true for viscous Newtonian fluids.

2. Model: stroke kinematics and fluid system

Experiments with *C. reinhardtii* in viscoelastic fluids were performed using dilute polymeric solutions [15], which were prepared by dissolving small amounts of a high molecular weight (MW) flexible polymer (polyacrylamide, 18×10^6 MW) in M1 buffer solution. The polymer concentration in solution ranged from 5 to 80 ppm, resulting in fluid relaxation times that ranged from 6 ms to 0.12 s, respectively. The low polymer concentration minimized the effects of shear-thinning viscosity while the high MW of the polymer introduced elasticity in the fluid. Motile algae were then suspended in viscoelastic (and Newtonian) fluids. A small volume of this suspension was stretched to form a thin film (thickness ∼20 μm) using a wire-frame device. The motion of freely swimming *C. reinhardtii* and its swimming strokes were imaged in the thin film using an optical microscope and a high-speed camera. Results in Newtonian fluids (figure 1a) show the well-known power and recovery strokes that are characteristic of swimming *C. reinhardtii* [26,28]. Note that the beating form is mostly planar, which is confirmed by measuring the length of flagellum and the cell body rotation. Experiments in which the flagellum length deviated by more than 10% of its original size and/or significant body rotation was observed were discarded. More details on fluid preparation, rheology and experimental methods are available in [15].

We used a three-dimensional computational model of the *C. reinhardtii* cell swimming in both Newtonian and viscoelastic fluids. Other theoretical studies of *C. reinhardtii* have been performed using both idealized strokes [31,32] and strokes based on experimental data [33], although the focus was on Newtonian fluids while the present study focused on viscoelasticity. Our approach and method of fitting to data are similar to [33]. The swimmer body is ellipsoidal with two symmetric flagella that execute a planar stroke in the mid-plane of the body. The kinematics of the stroke are prescribed, independent of the fluid rheology, and they are based on our experimental measurements of the flagellar kinematics in fluids with different rheologies [15]. Our model 'Newtonian stroke' is based on the kinematic data from about seven cycles of a single representative swimmer in a Newtonian fluid with viscosity 2.6 cP. The model 'viscoelastic stroke' is based on the kinematic data from about seven cycles of a single representative swimmer in a polymeric solution with similar viscosity (2.5 cP) and relaxation time corresponding to a Deborah number $De = \lambda/T = 2$. The Deborah number is used to quantify the effects of elasticity and is defined as the ratio of the fluid relaxation time λ to the period of the stroke T; note that $De = 0$ for Newtonian fluids.

We generate a model planar stroke by fitting the experimental data of the positions of the flagella from each stroke pattern to a system of model functions of the form

$$\left. \begin{array}{l} X_i(t,s) = M_i(s) + A_i(s)\cos\left(\dfrac{2\pi t}{T} + \phi_i(s)\right), \quad i = 1, 2 \\ \\ \text{and} \quad X_3(t,s) = 0. \end{array} \right\}$$

$$(2.1)$$

Here X_1, X_2 and X_3 are the Cartesian components of the flagellum's location $\mathbf{X}$, t is time and s is the arclength coordinate on each flagellum. The Fourier transform of the experimental shape data shows a strong peak at one frequency, and hence we fit the data using a single mode. The mean value $M_i(s)$,
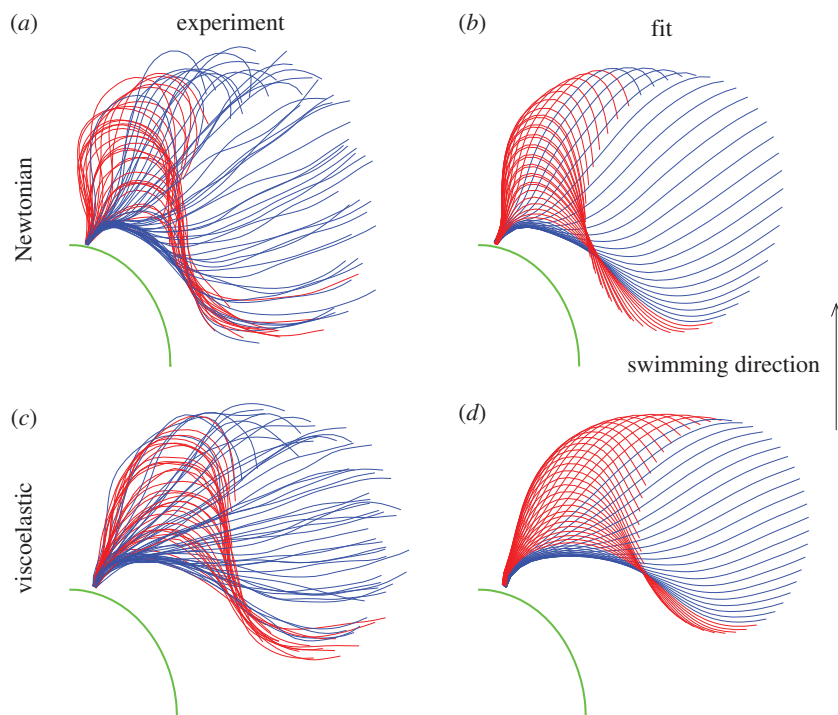
Figure 1. Flagellar stroke patterns corresponding to a swimmer in a Newtonian (a,b) and viscoelastic (c,d) fluid. (a,c) Experimental data and (b,d) fit. Power stroke (blue) and return stroke (red) are distinguished. The experimental data displayed consist of almost seven full cycles for each cell, and the model data shown are for one full cycle.

amplitude $A_i(s)$ and phase $\phi_i(s)$ are generated using cubic spline interpolation. In figure 1, we show both the raw data (consisting of almost seven full cycles) and single period of the model stroke sampled at a high time rate for each stroke, highlighting the power (in blue) and return (in red) strokes. The experimental data and the values of $M_i(s)$, $A_i(s)$ and $\phi_i(s)$ used to construct the splines are available from [34]. For more details about the fitting procedure, see the electronic supplementary material.

We use Lagrangian coordinates to describe the swimmer's position, velocity and forces, and Eulerian coordinates to describe the fluid velocity, stress and pressure. We use ideas from the immersed boundary method to couple the Eulerian and Lagrangian variables [35]. The shape of the swimmer is prescribed in a fixed body frame. In the laboratory frame, the position is given by $\mathbf{X} = \mathbf{X}_P(s, t) + \mathbf{X}_0(t)$, where $\mathbf{X}_0(t)$ is the translation of the origin in the body frame. The velocity of the swimmer is $\partial_t \mathbf{X} = \mathbf{U}_P + \mathbf{U}_T$, where $\mathbf{U}_P$ is the prescribed velocity in the body frame and $\mathbf{U}_T$ is the translational velocity of the swimmer. Given the current position of the swimmer and the prescribed velocity in the laboratory frame, we simultaneously solve for the fluid velocity and the translational velocity of the swimmer. The cell body is taken as an ellipsoid with diameters 10 μm, 10 μm and 12 μm, the longer axis being aligned with the swimming direction. The flagellum length of *C. reinhardtii* is typically between 10 and 14 μm. Owing to the variance of individuals used in experiments, each experimental dataset contains the kinematics of a flagellum with a slightly different length. In order to make a fair comparison in the model, we rescale the length of our model strokes so that each model stroke has an identical flagellum length. We pick the average arc length throughout a stroke period of our model viscoelastic stroke with $De = 2$, which is 12.5 μm, as a 'standard length', and then rescale all other model strokes so that each of them has the same average arc length.

The fluid is described by the Stokes equations with the addition of a polymer stress tensor, $\boldsymbol{\tau}_P$, to account for the viscoelastic stresses

$$\eta_s \Delta \mathbf{u} - \nabla p + \nabla \cdot \boldsymbol{\tau}_P + \mathbf{f} = 0 \qquad (2.2)$$

and

$$\nabla \cdot \mathbf{u} = 0, \qquad (2.3)$$

where $\mathbf{u}$ is the fluid velocity, p is the fluid pressure and η_s is the solvent viscosity. The external force density, $\mathbf{f}$, is used to enforce the prescribed shape of the swimmer.

As mentioned above, the experimentally derived 'Newtonian' and 'viscoelastic' strokes are obtained in fluids of similar viscosity (2.6 versus 2.5 cP) and the main difference is the fluid elastic stresses present in the viscoelastic experiments ($De = 2$). Here, we use the Oldroyd-B model [36], which is a relatively simple nonlinear constitutive model widely used to simulate viscoelastic flows. We note that the Oldroyd-B model has constant viscosity, while the fluids from our experiments show a small amount of shear thinning as described in [15]. Our intention is not to match the rheology from the experiments exactly, but rather isolate and investigate the effects of elasticity on the swimming behaviour of *C. reinhardtii*. The Oldroyd-B model can be derived from a description of the polymers as dumbbells connected by linear springs. The fluid flow stretches the polymers, giving a memory of past deformations which then relaxes on some characteristic time scale. The deformation of the polymers feeds back on the fluid through a macroscopic extra stress tensor, or polymer stress tensor, given by an average of distribution of polymer configurations. In the Oldroyd-B model the polymer stress tensor is related to a conformation tensor, $\boldsymbol{\sigma}$, describing the average distribution and orientation of polymers

$$\boldsymbol{\tau}_P = \frac{\eta_P}{\lambda}(\boldsymbol{\sigma} - \mathbf{I}), \qquad (2.4)$$
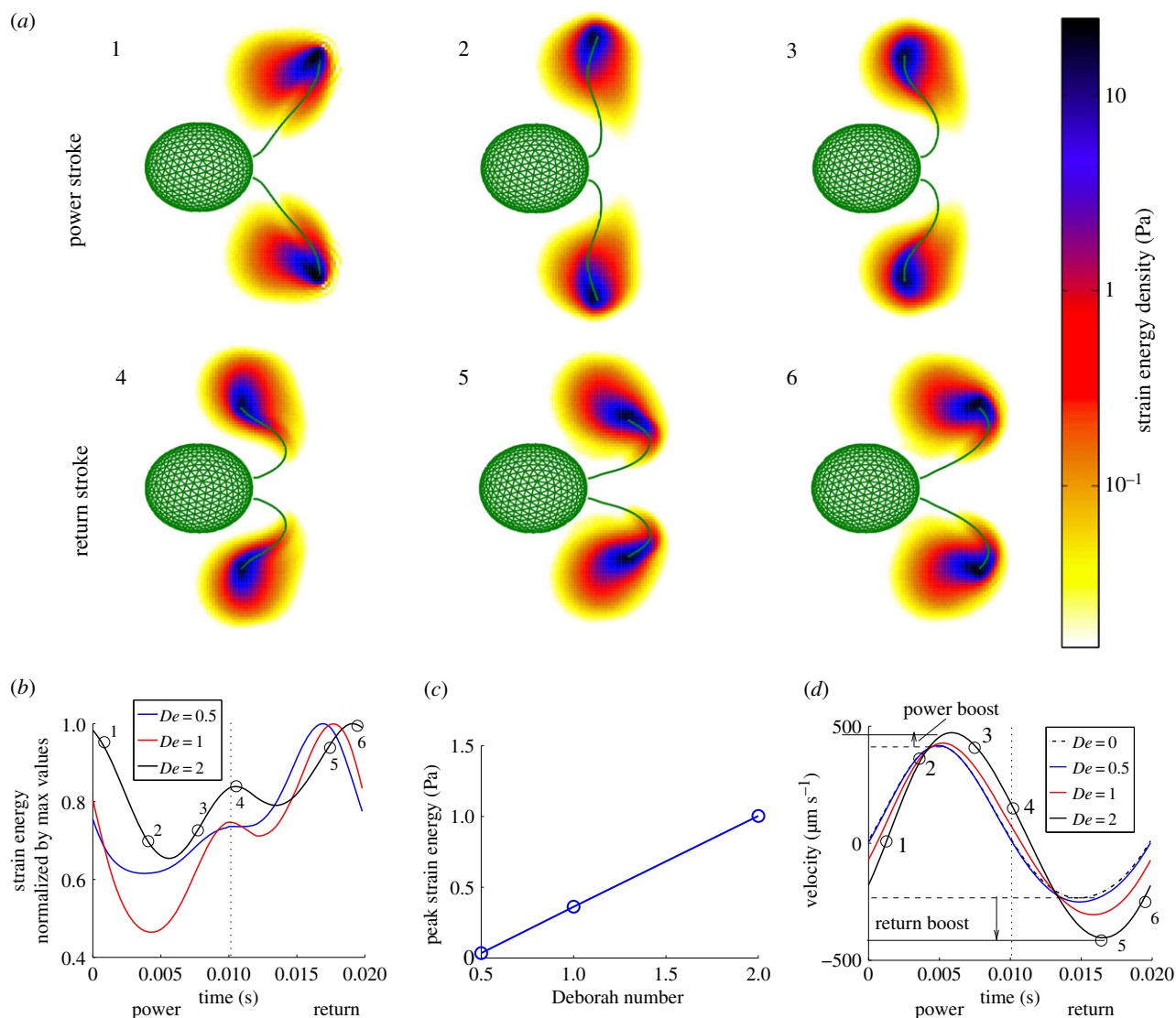
Figure 2. (a) Snapshots of strain energy density in the central plane for $De = 2$ using the viscoelastic stroke; the time points for these images are marked in (b) and (d) with the labels 1−6. (b) Root mean square of the strain energy density in the midplane as a function of time for different De normalized by maximum values. (c) Maximum values of the root mean square of the strain energy density in the midplane, used to normalize (b). (d) Velocity over one stroke for different De. The power and return boosts are marked for $De = 2$.

where η_P is the polymer viscosity and λ is the fluid relaxation time. The conformation tensor evolves according to

$$\partial_t \boldsymbol{\sigma} + \mathbf{u} \cdot \nabla \boldsymbol{\sigma} - \left(\boldsymbol{\sigma} \cdot \nabla \mathbf{u} + \nabla \mathbf{u}^{\mathrm{T}} \cdot \boldsymbol{\sigma} \right)$$
$$= -\frac{1}{\lambda}(\boldsymbol{\sigma} - \mathbf{I}) + \varepsilon \Delta \boldsymbol{\sigma}. \tag{2.5}$$

A numerical regularization term, $\varepsilon \Delta \boldsymbol{\sigma}$, is added [37,38] where $\varepsilon \propto (\Delta x)^2$ for grid spacing Δx; thus in the limit $\Delta x \to 0$ this regularized model converges to the Oldroyd-B model. The elastic strain energy density is the trace of the stress tensor, $\mathrm{Tr}(\boldsymbol{\tau_P})$.

Full details of the model equations and numerical methods, including validation, are given in appendix A.

3. Dissecting the effects of fluid elasticity and stroke

In biological experiments, the cell's swimming stroke changes in response to changes in fluid rheology, which makes it difficult to interpret and use experimental data alone to understand the role of fluid elasticity in swimming. Here, the relative roles of swimming stroke and fluid rheology are isolated by varying

them separately using simulations and experimental data. We begin by extracting the cell's swimming strokes from experiments in Newtonian and viscoelastic fluids (figure 1). Cells with these different swimming strokes are then investigated in fluids in which the polymer relaxation time λ, and, consequently, the Deborah number $De = \lambda/T$, is systematically varied with the stroke period T held fixed.

3.1. Elastic stress and swimming speed during a single stroke

Fluid elastic (polymeric) stresses are an important quantity that is difficult to obtain in experiments, but can be resolved in simulations. In this section, we use the viscoelastic stroke (figure 1d) obtained from experiments and vary the fluid relaxation time λ and consequently De in simulations. In figure 2a, we show snapshots of the fluid strain energy density in the central swimming plane at $De = 2$ (the Deborah number of the experiment from which this stroke was derived). The strain energy density is the trace of the elastic stress tensor and it gives a measure of the size of the elastic stress. It is notable that high stress is concentrated only near the distal tips of the
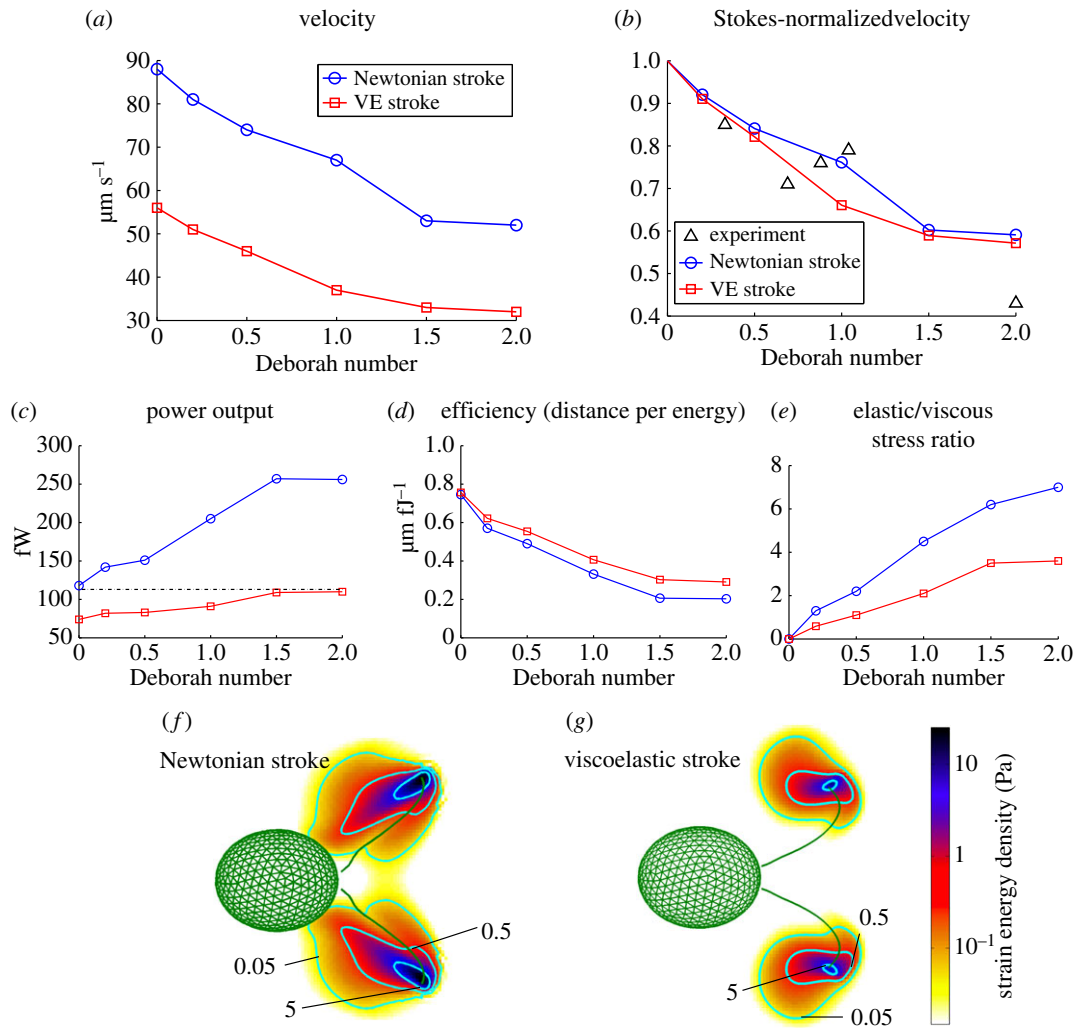
Figure 3. (a) Average speed for Newtonian and viscoelastic strokes. (b) Average speed normalized by the $De = 0$ speed in experiments and in the model. (c) Average power output. (d) Swimming efficiencies measured as the ratio of average speed to average power. (e) Average ratio of elastic stress to viscous stress. (f) Snapshot of the strain energy density induced by the Newtonian stroke, at peak value. (g) Snapshot of the strain energy density induced by the viscoelastic stroke in the same phase as (f).

flagella, contrary to the conjecture in [15] that high-stress regions develop near both ends of the flagella as well as near the body. The flagellar tips are travelling three to four times faster than the cell body (see the electronic supplementary material), but this speed difference alone cannot account for the orders of magnitude difference in elastic stress found near the flagellar tips and the cell body.

In figure 2b, we show the time course of the spatially averaged strain energy density throughout the entire stroke for different Deborah numbers. The elastic stress is generally lower during the power stroke than during the return stroke for all Deborah numbers. The lowest stresses occur near the middle of the power stroke, and the highest stresses occur towards the end of the return stroke. The magnitude of the stress increases monotonically with Deborah number (figure 2c).

Next, we investigate the effects of accumulated stresses on the cell propulsion speed. The velocity of the swimmer over the course of a complete stroke is shown in figure 2d for different Deborah numbers. We see that fluid elasticity boosts the speed of both the power and return strokes and produces a phase shift in which the peak velocities occur later in time. The size of the boosts and the extent of the phase shifts both increase with De. The speed of the return stroke as the cell moves backwards is boosted to a greater extent than the speed of the power stroke when the cell is moving forwards.

We conjecture that the accumulated fluid elastic stress is primarily responsible for the speed boost, which is supported by the observation of larger elastic stress and larger speed enhancements during the return stroke. An elastic slow-down in the net swimming speed results from the fact that the return stroke experiences a stronger speed boost (going backwards) than the power stroke (figure 2d), and as De increases the size of the speed enhancements increases.

3.2. Comparing Newtonian and viscoelastic strokes

Next we compare the swimming performance of the viscoelastic stroke with that of the Newtonian stroke (figure 1b) using model fluids that range from $De = 0$ (Newtonian) to $De = 2$. The results of the previous section (spatial–temporal stress distributions and effect of elasticity on swimming speed) do not change qualitatively when the Newtonian stroke is used in place of the viscoelastic stroke (see the electronic supplementary material). Here, we examine time-averaged quantities to assess the swimming performance of the two strokes. The Newtonian stroke yields swimming speeds 60% faster than those of the viscoelastic stroke (figure 3a), but both speeds decrease with increasing Deborah number at about the same rate, which is evident after normalizing by the $De = 0$ (i.e. Newtonian) swimming speed (figure 3b). Also shown in this figure are

experimental data from [15], and although each *De* involves different kinematics the speed decrease with *De* shows the same trend as the model. By contrast, the power consumption (figure 3*c*) increases much more substantially with increasing elasticity for the Newtonian stroke than for the viscoelastic stroke. Comparing the results for $De = 2$ with those for $De = 0$, we see the Newtonian stroke uses over twice as much power, while the increase from the viscoelastic stroke is only approximately 50%.

We compute the instantaneous power output by integrating $\mathbf{F} \cdot \mathbf{U}$ over the swimmer body and flagella, where $\mathbf{U}$ is the pointwise velocity of the swimmer and $\mathbf{F}$ is the force density on the swimmer body and flagella. The power consumption reported in figure 3*c* is the average power in one period. A similar mechanical measurement of the average power output per period was reported in [29] to be approximately 5 fW based on two-dimensional measurements of the fluid flows in the swimmer's midplane with a resolution of 3 μm. We attribute our higher power estimate to the fact that it involves the full three-dimensional flow field with submicrometre spatial resolution. Our value of 110 fW for the average power consumption corresponds to approximately 2×10^6 ATP s^{-1} (using 54×10^{-21} J/ATP [39]) or 10^6 ATP s^{-1} per flagellum, which agrees with the measured value of 0.97×10^6 ATP s^{-1} [40].

Figure 3*d* shows the swimming efficiency, quantified as the ratio of average speed to average power (distance travelled per energy dissipated), for both strokes. We note that this measure of efficiency is different from the typical measure for microorganism locomotion in viscous fluids, which is the ratio of the power needed to drag the body at the average swimming speed to the power dissipated during swimming [41]. For viscoelastic fluids, the drag force is a nonlinear function of the velocity and it depends on the time history of the motion. Thus, it is not clear that normalizing by the power needed for steady motion is appropriate, and so we use the dimensional distance per energy dissipated. In a Newtonian fluid ($De = 0$), the two strokes have comparable efficiencies. Both strokes result in lower efficiency as fluid elasticity increases, but the greater increase in power needed to maintain the Newtonian stroke with increasing elasticity (figure 3*c*) leads to less efficient swimming in a viscoelastic fluid.

We also find that the Newtonian stroke induces higher elastic stress, as shown in figure 3*e*−*g*. These elevated stresses are responsible for the larger power needed by the swimmers using the Newtonian stroke. In the presence of fluid elasticity, the cell requires more power to maintain a fixed stroke, suggesting that the swimmer may change its stroke to the fluid properties based on energy availability. In particular, we note from figure 3*c* that it requires a similar amount of power to maintain the Newtonian stroke at $De = 0$ as the viscoelastic stroke at $De = 2$ (the stroke was based on experiments at $De = 2$).

4. Mechanisms of asymmetric speed enhancements

Our simulations revealed that the stress accumulated during the return stroke is higher than the stress accumulated during the power stroke. Similarly, elasticity led to a larger enhancement of the swimming speed during the return stroke than during the power stroke. These observations motivate two questions. (i) How are the accumulated stresses related to

speed enhancements? (ii) Why is there an asymmetric stress response on power and return?

4.1. Speed enhancements from fluid memory

In our computational model, if the shape of the swimmer is suddenly fixed, the cell stops moving instantaneously in a Newtonian fluid (at zero Reynolds number) because the motion of the fluid and the translation of the cell are driven entirely by the changing shape of the flagella as all forces are equilibrated instantaneously. In a viscoelastic fluid, however, once the shape of the flagella is suddenly fixed, the swimmer continues to translate because as the accumulated elastic stresses relax they drive a flow. In figure 4*a*,*b*, we show the resulting velocity fields from the accumulated stress alone when the swimmer shape is suddenly fixed at its peak power and peak return strokes, respectively, at $De = 2$ for the viscoelastic stroke. The swimmer continues to move in the direction it was travelling when the stroke was frozen.

We quantify the effect of the accumulated elastic stress on the swimming speed by recording the initial coasting velocity (the initial velocity of the swimmer after the stroke is frozen) as a function of the stroke phase for a range of *De*, as shown in figure 4*c*. We find that increasing fluid memory (larger *De*) leads to larger initial coasting velocities, and the peak initial coasting velocity is 30–35% higher during the return stroke at $De = 2$.

In figure 4*d*, we plot the speed boost measured in our simulations (given by the difference between Newtonian and viscoelastic peak power or return velocities, as seen in figure 2*d*) together with the peak values of initial coasting velocity as a function of *De*. These two quantities show a similar dependence on *De* that strongly suggests that the accumulated stress is a significant factor in the speed boost. Further, from figure 2*d*, we see that the peak power and return enhancements occur with a time lag (phase shift) from the peak velocities in the Newtonian fluid, indicating that, as the stroke is beginning to slow down, fluid elasticity is continuing to accelerate the swimmer. Both this effective acceleration and the tendency of the swimmer to continue to move when the flagellar motion is suddenly stopped are the result of the accumulated elastic stress which provides an elastic memory effect.

4.2. Flagellar tip orientation and elastic stress

It is well known that net translation in a Newtonian fluid at zero Reynolds number requires non-reciprocal motion [42]. Much of our intuition regarding flagellated swimmers is based on the idea of resistive force theory (RFT) [43,44]. RFT relates the force and velocity on a segment of the flagellum by treating it as a locally straight cylinder and ignoring the long-range hydrodynamic interactions. The fundamental idea behind this theory is that organisms generate net motion by exploiting the fact that in a Newtonian fluid it requires less force to drag a long, thin cylinder along its axis than perpendicular to its axis [45].

In figure 5*a*,*d* we plot the flagellum shapes from the Newtonian and viscoelastic strokes, respectively, with the distal tip highlighted, and in figure 5*b*,*e* we plot the angle of the tip relative to the swimming direction. It is clear that the tip orientation during the power stroke is less aligned with the direction of motion than during the return stroke. This temporal asymmetry of the orientation of this segment of the flagellum generates more force, and thus velocity, during the power stroke than during the return stroke in a Newtonian fluid. Of course, the
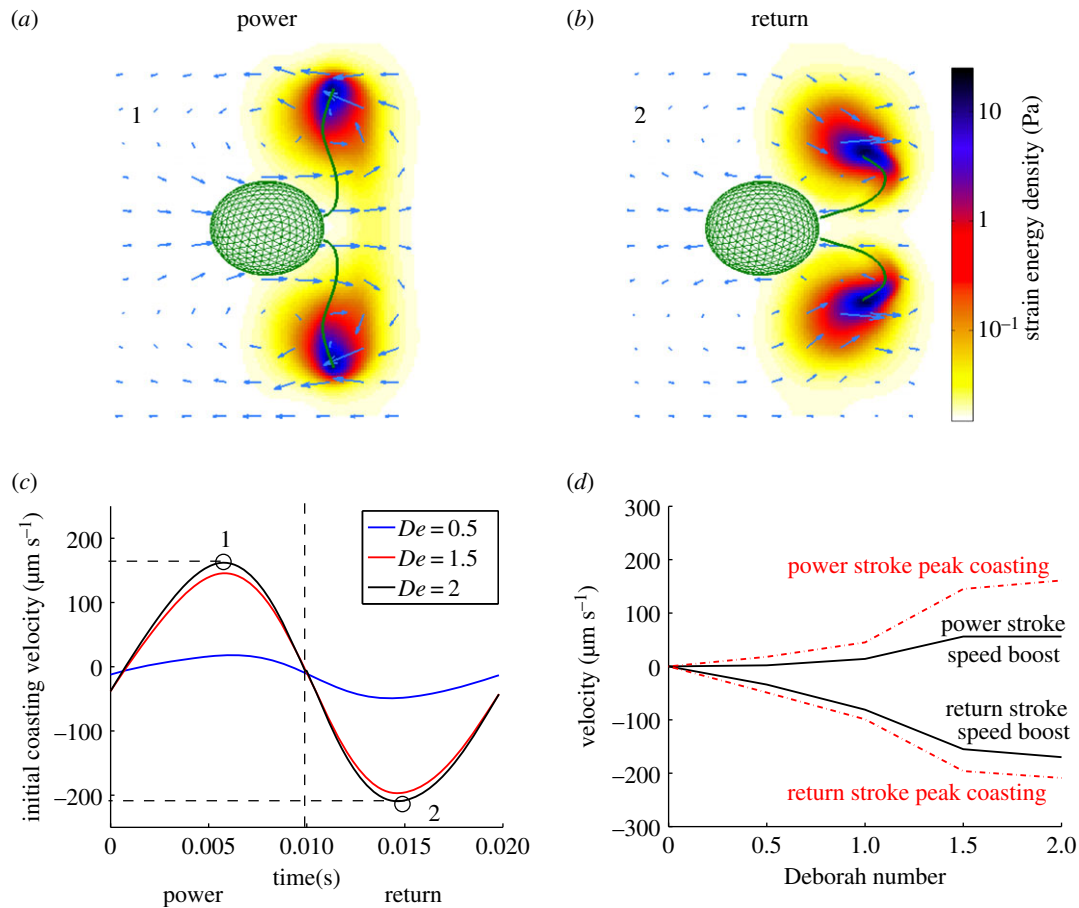
Figure 4. Flow field and accumulated elastic stress after the stroke is frozen for $De = 2$ for the viscoelastic stroke; (a) power stroke, (b) return stroke. (c) Initial coasting velocity; (d) peak initial coasting velocity and actual speed boost.

difference in shape of the entire flagellum during the return stroke and power stroke is responsible for generating motion, but we focus on the tip because that is where the large elastic stresses concentrate. Returning to figure 2, we observed that higher elastic stress is accumulated when the flagellar tip is oriented tangential to the direction of motion in the return stroke than when oriented normal to the direction of motion in the power stroke. This temporal asymmetry in elastic stress and the resultant speed boosts work against the advantages obtained by the breast-stroke motion, and are contrary to the expectations based on viscous fluid theory.

In order to gain insight into the effects of flagellar tip orientation in a viscoelastic fluid on swimming, we simulate a thin cylindrical rod travelling at a constant velocity both tangential and normal to its long axis and measure the elastic stress as a function of fluid elasticity. We use a rod length of $8\,\mu m$, and drag it at a constant velocity of $100\,\mu m\,s^{-1}$ (characteristic lengths and speeds of a free swimming alga) until the elastic stress is equilibrated. To characterize the strength of elasticity, we define a dimensionless Weissenberg number for this problem as $Wi = \lambda U_\infty / L$, where λ is the polymer relaxation time, U_∞ is the velocity of the rod and L is the length of the rod. The elastic strain energy density for a rod that is tangential and normal to a viscoelastic flow at $Wi = 7.5$ is shown in figure 6a,b, respectively. A region of very high elastic stress is found near the trailing tip of the rod moving in the tangential direction, while lower elastic stress is found near the rod moving in the normal direction. In figure 6c, we examine how the elastic stress in each orientation depends on Wi, and we find that the difference between the size of the elastic

stresses between the two rod orientations grows with increasing fluid elasticity.

Viscous stress and elastic stress have significantly different trends as the Weissenberg number increases (figure 6d). The viscous stress ratio (tangential to normal) is always less than 1, which agrees qualitatively with what we expect from viscous fluid theory, but the elastic stress ratio increases with Wi, and for sufficiently large Wi this ratio is larger than 1. Thus, the orientation asymmetry between power and return strokes, which enables swimming in viscous fluids, can induce higher fluid elastic stress and potentially hinder swimming in strongly elastic flows.

The orientation of the flagella during swimming changes continually throughout the stroke, and because viscoelastic stress is not instantaneously equilibrated the steady-state relationship between elastic stress and orientation does not completely explain elastic stress development during swimming. In figure 6e, we show how the elastic stress grows in time starting from rest at $Wi = 7.5$, and even on time scales below the relaxation time the elastic stress is larger for rods moving in the tangential direction than for rods moving in the normal direction. We conjecture that the difference in orientation of the tips of the flagella on power and return strokes contributes substantially to the higher elastic stress observed during the return stroke, and the fact that this effect is heightened for larger Wi also agrees well with the observed increase in peak elasticity as De increases in figure 2d. This conjecture is further supported by comparing tip motion in the Newtonian and viscoelastic strokes in figure 5; the tip of the Newtonian stroke is more aligned to the direction of motion, the amplitude of
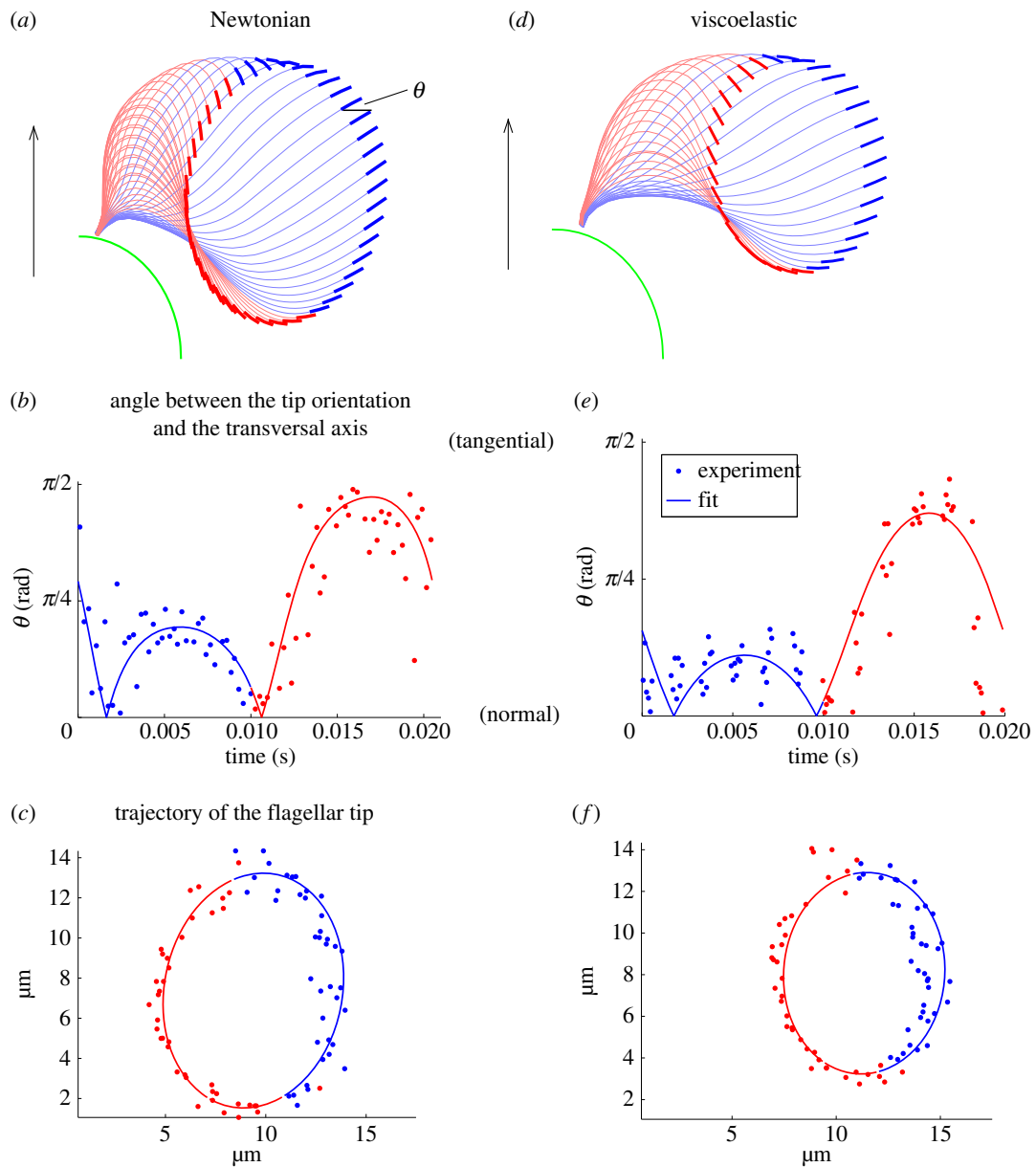
Figure 5. (a) The Newtonian stroke with the tip of a flagellum highlighted; (b) angle between the tangential direction of the flagellar tip and the axis perpendicular to the swimming direction for the Newtonian stroke, with both experimental and fit data displayed; (c) the trajectory of the flagellar tip from the Newtonian stroke; (d,f) counterparts of (a,c) for the viscoelastic stroke. Power stroke (blue) and return stroke (red) are distinguished.

the motion is larger and the resulting elastic stresses are larger (figure 3).

5. Discussion

Swimming microorganisms change their gait in response to changes in fluid rheology, which makes it difficult to understand the effects of fluid elasticity on swimming based on experimental measurements alone. Using our three-dimensional computational model with experimentally derived kinematics of swimmers in fluids with rheologies that are comparable to those used in our experiments, we separate the two effects and provide new insight into how fluid elasticity affects flagellated swimmers. By fixing the stroke and varying the fluid elasticity, we observed both the power and return stroke velocity increase with elasticity, but the speed on the return stroke was boosted to a greater extent, leading to a net slow-down in swimming speed (figure 2d). This trend is different from the experimental results

from [15], in which the power stroke speed appeared to be retarded by elasticity until a very high Deborah number, and the return stroke was enhanced only for $De > 2$. We attribute the difference in observations to the fact that in the experiments the stroke changes as the fluid elasticity changes. Using the computational model, we showed that the viscoelastic stroke itself leads to slower swimming than the Newtonian stroke in fluids with the same rheology. Thus the changes from elasticity in speed during the power and return strokes that we measured experimentally were the sum of two competing effects of a slow-down due to changing stroke and a speed-up from the development of elastic stress.

By comparing the swimming performances of a Newtonian and a viscoelastic stroke pattern in different fluids, we address whether the changes in gait that occur with rheology offer any advantage. We note that both strokes are similar to the predicted optimally efficient stroke in a Newtonian fluid [46]. Cells using the Newtonian stroke swim faster in all fluids. However, this higher speed comes at a cost as it requires
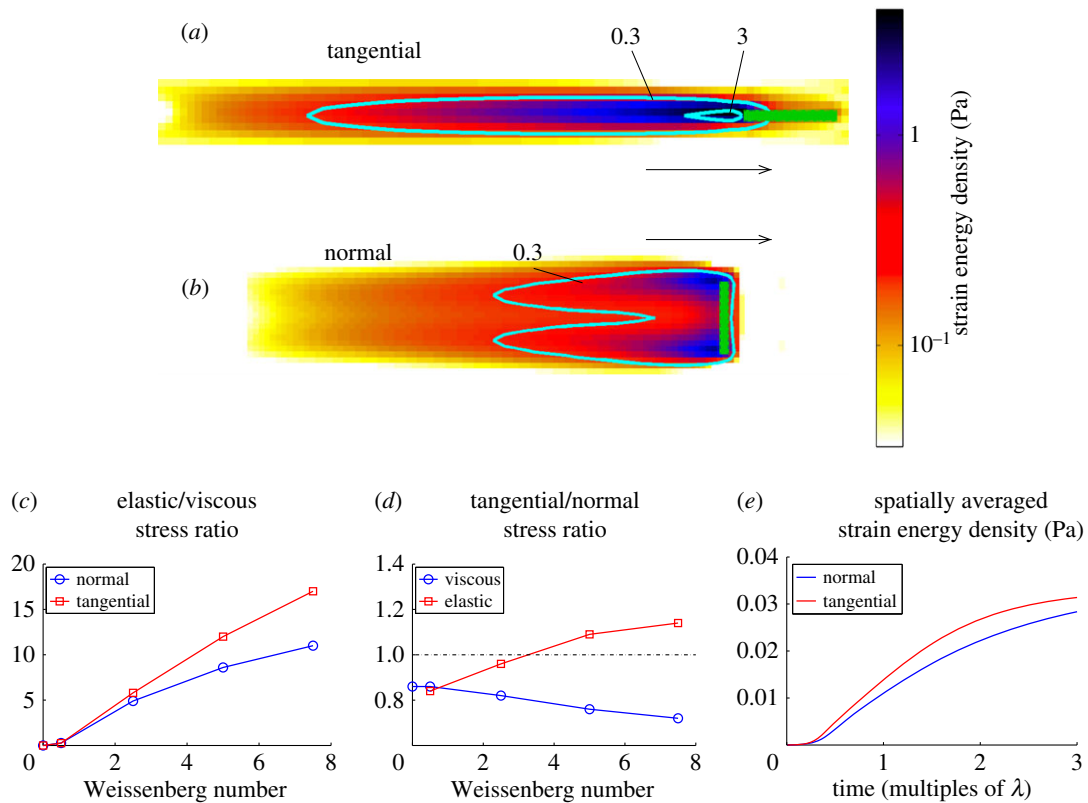
Figure 6. (*a*, *b*) Fluid strain energy density induced by a rod travelling tangential (*a*) and normal (*b*) to its long axis with $Wi = 7.5$; (*c*) ratio of elastic stress to viscous stress induced by travelling rods with different orientations; (*d*) ratio of stresses of the tangentially moving rod to the normally moving rod. (*e*) Spatial average of the strain energy density as a function of time starting from rest at $Wi = 7.5$.

more mechanical energy to maintain than the viscoelastic stroke as fluid elasticity increases. Thus the viscoelastic stroke is more efficient (measured as distance per energy dissipated) in fluids with high elasticity. It is notable that it requires a similar amount of power to maintain the Newtonian stroke at $De = 0$ as the viscoelastic stroke at $De = 2$, as shown in figure 3*b* (the stroke was based on experiments at $De = 2$). The value of the average power we obtain in these two cases is on a par with the energy usage by the organism as measured by ATP consumption [40]. These results suggest that the viscoelastic gait may result from the power limitations. The change to the gait in response to fluid elasticity yields more efficient swimming in viscoelastic fluids, although we note that *Chlamydomonas* do not swim in viscoelastic fluids in their natural environment. However, given the conserved internal structure of the eukaryotic axoneme, these results may be related to why similarly flagellated cells such as spermatozoa exhibit qualitatively different beat patterns in Newtonian and viscoelastic fluids [12].

It is difficult to measure the elastic stress in experiments [16,22,23], but it is essential to know what the elastic stresses are to interpret experimental observations. In [15], based on measured changes in flagellar kinematics with elasticity and previously measured flow fields from [29], we conjectured that elastic stresses accumulated near both the distal and proximal ends of the flagella and near the body, but our experiments alone did not give us the means to test this conjecture. One of the major results of the present study is that the elastic stresses concentrate only near the distal tips of flagella at all phases of a swimming stroke, and the stress accumulated on the return stroke is higher than the stress accumulated during the power stroke. These large tip stresses are reminiscent of those reported in previous two-dimensional computational studies of undulatory swimmers [18,20,47,48], but to date the effects

of localized elastic stress on swimming performances are poorly understood.

The initial coasting velocity provides a quantification of the effect of the large elastic stresses on the swimming speed. We observed that the initial coasting velocity and speed enhancement of the power and return strokes follow the same increasing trend in fluid elasticity. These accumulated stresses provide an elastic memory effect that continues to increase the speed even as the speed of the stroke begins to decrease. This elastic memory effect together with the temporal asymmetry of the larger stresses on the return stroke lead to an overall slow-down in swimming as the elasticity is increased for a fixed stroke.

We conjecture that the asymmetry of the orientation of flagellar tips between the power and return stroke leads to the higher elastic stress in the return stroke (figure 6), which is supported by our simulations and analysis (see the electronic supplementary material) of a thin cylinder moving in viscoelastic fluids with different orientations. Our results reveal a fundamental difference between viscous and elastic effects in the relationship between orientation and stress. In a Newtonian fluid, the larger viscous stress associated with motion normal to the cylinder axis compared with motion tangential to the cylinder axis is essential to gaining net displacement for flagellated swimmers. In viscoelastic fluids, however, this stress asymmetry is reversed, which leads to the higher elastic stress accumulation during the return stroke compared with the power stroke, causing a decrease in overall swimming speed.

The orientation-dependent elastic stress asymmetry is likely to be important in understanding other microorganism motility and flagellar motion in complex fluids. It is difficult, however, to generalize from one organism to another as it

has been shown that the effect of fluid elasticity on swimming speed is gait dependent [20,49,50]. The particular motion studied here has similarities to pulmonary cilia, which beat in a layered fluid consisting of the periciliary liquid surrounding the base of the cilia and a mucus layer on top which is more viscous and strongly elastic [51,52]. Cilia extend into the mucus layer during the power stroke, but recoil to stay within the watery liquid layer during the return stroke. While it is not surprising that this asymmetry would be beneficial for transport, our results suggest that ducking the more elastic mucus on the return stroke is essential to avoid large elastic stress that works against transport. Finally, we note that, while the present study focuses on purely elastic effects using the Oldroyd-B model, complex fluids often display rate-dependent rheological properties which are not captured by the model. Nevertheless, it is known that large stresses still accumulate in regions of high stretching (and gradients) even in models with these additional nonlinearities [53–56], and the qualitative results showing both the concentration of elastic stress at tips as well as asymmetric accumulation that depends on tip orientation are not expected to change.

Appendix A. Numerical method

In this section, we describe our numerical formulation to solve the coupled swimmer–fluid system. Our method is similar to [33] in that the kinematics of the flagellum are prescribed exactly, and the force density and swimming speed are solved for simultaneously. However, in [33] they use the method of regularized Stokeslets [57], which is similar to boundary integral methods that require the linearity of the Stokes equations and does not generalize to viscoelastic fluids. Because the viscoelastic stress introduces additional body forces distributed throughout the fluid domain, the equations of motion cannot be reduced to integral equations on the swimmer body alone. We use the immersed boundary method [35], which has been used for simulations of flexible undulatory swimmers in viscoelastic fluids [18,20,47,48] as well as for simulating *C. reinhardtii* swimming in Newtonian fluids [32]. We use Lagrangian coordinates to describe the swimmer's position, velocity and forces, and Eulerian coordinates to describe the fluid velocity, stress and pressure. We use the framework of the immersed boundary method to compute the Eulerian and Lagrangian variables [35]. Specifically, the force density on the swimmer is related to the force applied to the fluid by

$$\mathbf{f}(\mathbf{x}, t) = \mathcal{S}\mathbf{F} = \int_{\text{swimmer}} \mathbf{F}(\mathbf{s}, t)\delta(\mathbf{x} - \mathbf{X}(\mathbf{s}, t))\,\mathrm{d}\mathbf{s}, \qquad \text{(A 1)}$$

where we use the notation $\mathcal{S}$ to denote the spreading operator, which maps Lagrangian variables to Eulerian variables.

Similarly, the adjoint operator $\mathcal{S}^*$ maps the Eulerian fluid velocity to the velocity on the swimmer by

$$\mathbf{U}(\mathbf{s}, t) = \mathcal{S}^*\mathbf{u} = \int_{\text{fluid}} \mathbf{u}(\mathbf{x}, t)\delta(\mathbf{x} - \mathbf{X}(\mathbf{s}, t))\,\mathrm{d}\mathbf{x}. \qquad \text{(A 2)}$$

In the discretization of the transfer operators defined in equations (A 1) and (A 2), we use the standard four-point regularized delta function [35].

In each time step of the simulation, we alternately advance the conformation tensor and the fluid/body system. Given the current fluid velocity field ($\mathbf{u}$), we evolve the conformation tensor ($\boldsymbol{\sigma}$) according to equation (2.5), from which we compute the polymer stress tensor ($\boldsymbol{\tau}_\mathbf{p}$) from (2.4). Given the updated polymer stress tensor and the prescribed velocity of the flagella and cell body in the body frame ($\mathbf{U}_\mathrm{P}$), we then simultaneously solve for the fluid velocity ($\mathbf{u}$) and pressure (p), the translational velocity of the swimmer body ($\mathbf{U}_\mathrm{T}$) and fluid forces on the swimmer ($\mathbf{F}$), which satisfy

$$\eta_\mathrm{s}\Delta\mathbf{u} - \nabla p + \mathcal{S}\mathbf{F} = -\nabla \cdot \boldsymbol{\tau}_\mathbf{p}, \qquad \text{(A 3)}$$

$$\nabla \cdot \mathbf{u} = 0, \qquad \text{(A 4)}$$

$$\mathcal{S}^*\mathbf{u} - \mathbf{U}_\mathrm{T} = \mathbf{U}_\mathrm{P} \qquad \text{(A 5)}$$

and

$$\int_{\text{swimmer}} \mathbf{F}\,\mathrm{d}\mathbf{s} = \mathbf{0}. \qquad \text{(A 6)}$$

Equation (A 5) determines that the swimmer moves with the local fluid velocity (i.e. there is no slip on the body surface), and equation (A 6) requires that the net force on the swimmer is zero. To solve equations (A 3)–(A 6), we eliminate the velocity and pressure, and first solve the much smaller system for the body forces and translational velocity,

$$\mathcal{S}^*\mathcal{L}^{-1}\mathcal{S}\mathbf{F} - \mathbf{U}_\mathrm{T} = \mathbf{U}_\mathrm{P} - \mathcal{S}^*\mathcal{L}^{-1}\nabla \cdot \boldsymbol{\tau}_\mathbf{p} \qquad \text{(A 7)}$$

and

$$\int_{\text{swimmer}} \mathbf{F}\,\mathrm{d}\mathbf{s} = \mathbf{0}, \qquad \text{(A 8)}$$

where $\mathcal{L}$ is the Stokes operator that maps a fluid velocity to the applied forces. After solving this system for the translational velocity and the force on the swimmer, we use these quantities to update the body position in the laboratory frame and the fluid velocity field to complete a time step.

The fluid domain is taken as a periodic cube with side lengths $40\,\mu\mathrm{m}$, which is discretized with 128 points in each direction. Each flagellum is discretized with 27 grid points along its central line, and the body is discretized using a set of minimum energy interpolation points on the sphere [58], where neighbouring points are approximately equally spaced. We use the Fourier spectral method to discretize the spatial operators. Equations (A 7) and (A 8) are solved using the conjugate gradient method, which is preconditioned using the method of regularized Stokeslets [57] to approximate the mobility operator $\mathcal{S}^*\mathcal{L}^{-1}\mathcal{S}$. Equation (2.5) for the conformation tensor is discretized in time using a Crank–Nicholson–Adams–Bashforth scheme (AB for the nonlinear terms), with the diffusion coefficient $\varepsilon = 8\Delta x^2/T$, where T is the stroke period and Δx is the mesh spacing. We use a time step $\Delta t = \frac{1}{60}$ ms, and fix the viscosity ratio $\eta_\mathrm{p}/\eta_\mathrm{s} = 0.2$.

We run all the simulations until the difference in average speeds between two successive periods falls below 5%, at which time the elastic stress field is approximately periodic
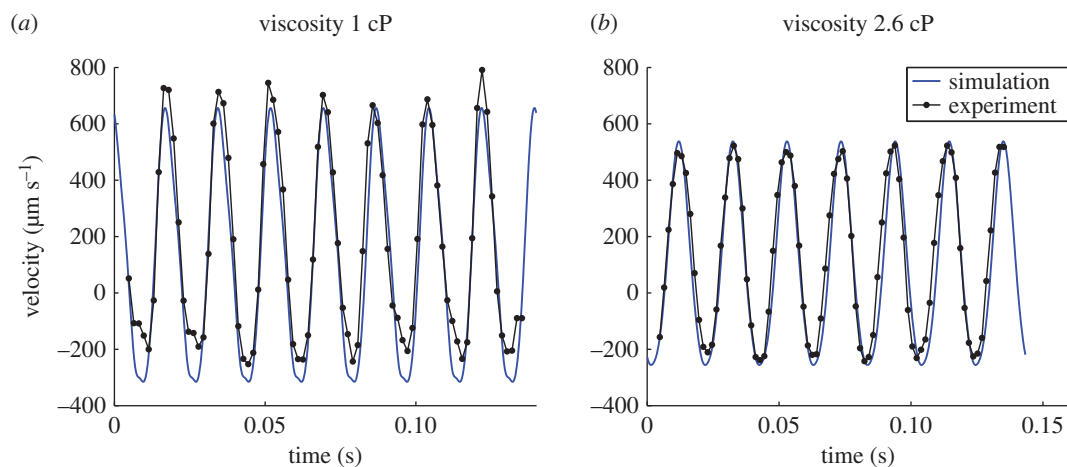
Figure 7. Swimming velocities from simulations and experiments in a Newtonian fluid for two different viscosities (a) 1 cP and (b) 2.6 cP. The kinematic data for viscosity 2.6 cP are those which are used for the model Newtonian stroke.

in time. The strain energy, elastic stress and viscous stress averages are computed over the entire three-dimensional computational domain.

We validate the model by comparing the swimming velocities from our simulations with the experiments on which the stroke was based. In figure 7, we plot the experimentally measured swimming velocities for cells swimming in

Newtonian fluids of two different viscosities along with the velocities produced by our simulations using strokes fitted from the same datasets. The 'Newtonian stroke' used throughout this paper is based on the data corresponding to viscosity 2.6 cP. In the electronic supplementary material, we show a similar comparison between the experiment and the simulations at $De = 2$.

References

1. Huang HW, Sakar MS, Petruska AJ, Pane S, Nelson BJ. 2016 Soft micromachines with programmable motility and morphology. *Nat. Commun.* **7**, 12263. (doi:10.1038/ncomms12263)

2. Ahmed D, Baasch T, Jang B, Pane S, Dual J, Nelson BJ. 2016 Artificial swimmers propelled by acoustically activated flagella. *Nano Lett.* **16**, 4968–4974. (doi:10.1021/acs.nanolett.6b01601)

3. Palagi S et al. 2016 Structured light enables biomimetic swimming and versatile locomotion of photoresponsive soft microrobots. *Nat. Mater.* **15**, 647–653. (doi:10.1038/nmat4569)

4. Ghosh A, Fischer P. 2009 Controlled propulsion of artificial magnetic nanostructured propellers. *Nano Lett.* **9**, 2243–2245. (doi:10.1021/nl900186w)

5. Koo OM, Rubinstein I, Onyuksel H. 2005 Role of nanotechnology in targeted drug delivery and imaging: a concise review. *Nanomed. Nanotechnol. Biol. Med.* **1**, 193–212. (doi:10.1016/j.nano.2005.06.004)

6. Sakar MS, Eyckmans J, Pieters R, Eberli D, Nelson BJ, Chen CS. 2016 Cellular forces and matrix assembly coordinate fibrous tissue repair. *Nat. Commun.* **7**, 11036. (doi:10.1038/ncomms11036)

7. Ding Y, Qiu FM, Solvas XCI, Chiu FWY, Nelson BJ, deMello A. 2016 Microfluidic-based droplet and cell manipulations using artificial bacterial flagella. *Micromachines* **7**, 25. (doi:10.3390/mi7020025)

8. Fauci LJ, Dillon R. 2006 Biofluidmechanics of reproduction. *Annu. Rev. Fluid Mech.* **38**, 371–394. (doi:10.1146/annurev.fluid.37.061903.175725)

9. Suarez S, Pacey A. 2006 Sperm transport in the female reproductive tract. *Hum. Reprod. Update* **12**, 23–37. (doi:10.1093/humupd/dmi047)

10. Celli JP et al. 2009 Helicobacter pylori moves through mucus by reducing mucin viscoelasticity. *Proc. Natl Acad. Sci. USA* **106**, 14 321–14 326. (doi:10.1073/pnas.0903438106)

11. Jimenez-Sanchez C, Wick LY, Cantos M, Ortega-Calvo JJ. 2015 Impact of dissolved organic matter on bacterial tactic motility, attachment, and transport. *Environ. Sci. Technol.* **49**, 4498–4505. (doi:10.1021/es5056484)

12. Suarez S, Dai X. 1992 Hyperactivation enhances mouse sperm capacity for penetrating viscoelastic media. *Biol. Reprod.* **46**, 686–691. (doi:10.1095/biolreprod46.4.686)

13. Lauga E. 2007 Propulsion in a viscoelastic fluid. *Phys. Fluids* **19**, 083104. (doi:10.1063/1.2751388)

14. Martinez VA, Schwarz-Linek J, Reufer M, Wilson LG, Morozov AN, Poon WCK. 2014 Flagellated bacterial motility in polymer solutions. *Proc. Natl Acad. Sci. USA* **111**, 17 771–17 776. (doi:10.1073/pnas.1415460111)

15. Qin B, Gopinath A, Yang J, Gollub JP, Arratia PE. 2015 Flagellar kinematics and swimming of algal cells in viscoelastic fluids. *Sci. Rep.* **5**, 9190. (doi:10.1038/srep09190)

16. Shen X, Arratia PE. 2011 Undulatory swimming in viscoelastic fluids. *Phys. Rev. Lett.* **106**, 208101. (doi:10.1103/PhysRevLett.106.208101)

17. Fu HC, Wolgemuth CW, Powers TR. 2009 Swimming speeds of filaments in nonlinearly viscoelastic fluids. *Phys. Fluids* **21**, 033102. (doi:10.1063/1.3086320)

18. Teran J, Fauci L, Shelley M. 2010 Viscoelastic fluid response can increase the speed and efficiency of a

free swimmer. *Phys. Rev. Lett.* **104**, 038101. (doi:10.1103/PhysRevLett.104.038101)

19. Zhu L, Lauga E, Brandt L. 2012 Self-propulsion in viscoelastic fluids: pushers versus pullers. *Phys. Fluids* **24**, 051902. (doi:10.1063/1.4718446)

20. Thomases B, Guy RD. 2014 Mechanisms of elastic enhancement and hindrance for finite-length undulatory swimmers in viscoelastic fluids. *Phys. Rev. Lett.* **113**, 098102. (doi:10.1103/PhysRevLett.113.098102)

21. Spagnolie SE, Liu B, Powers TR. 2013 Locomotion of helical bodies in viscoelastic fluids: enhanced swimming at large helical amplitudes. *Phys. Rev. Lett.* **111**, 068101. (doi:10.1103/PhysRevLett.111.068101)

22. Liu B, Powers TR, Breuer KS. 2011 Force-free swimming of a model helical flagellum in viscoelastic fluids. *Proc. Natl Acad. Sci. USA* **108**, 19 516–19 520. (doi:10.1073/pnas.1113082108)

23. Espinosa-Garcia J, Lauga E, Zenit R. 2013 Fluid elasticity increases the locomotion of flexible swimmers. *Phys. Fluids* **25**, 031701. (doi:10.1063/1.4795166)

24. Patteson AE, Gopinath A, Goulian M, Arratia PE. 2015 Running and tumbling with *E. coli* in polymeric solutions. *Sci. Rep.* **5**, 15761. (doi:10.1038/srep15761)

25. Fu HC, Powers TR, Wolgemuth CW. 2007 Theory of swimming filaments in viscoelastic media. *Phys. Rev. Lett.* **99**, 258101. (doi:10.1103/PhysRevLett.99.258101)

26. Goldstein RE. 2015 Green algae as model organisms for biological fluid dynamics. *Annu. Rev. Fluid Mech.*

47, 343 – 375. (doi:10.1146/annurev-fluid-010313-141426)

27. Harris EH. 1999 *The Chlamydomonas sourcebook*. New York, NY: Academic Press.

28. Ruffer U, Nultsch W. 1985 High-speed cinematographic analysis of the movement of Chlamydomonas. *Cell Motil. Cytoskeleton* **5**, 251 – 263. (doi:10.1002/cm.970050307)

29. Guasto JS, Johnson KA, Gollub JP. 2010 Oscillatory flows induced by microorganisms swimming in two dimensions. *Phys. Rev. Lett.* **105**, 168102. (doi:10.1103/PhysRevLett.105.168102)

30. Drescher K, Goldstein RE, Michel N, Polin M, Tuval I. 2010 Direct measurement of the flow field around swimming microorganisms. *Phys. Rev. Lett.* **105**, 168101. (doi:10.1103/PhysRevLett.105.168101)

31. Jones MS, Baron LL, Pedley TJ. 1994 Biflagellate gyrotaxis in a shear flow. *J. Fluid Mech.* **281**, 137 – 158. (doi:10.1017/S002211209400306X)

32. Fauci LJ. 1993 Computational modeling of the swimming of biflagellated algal cells. *Contemp. Math.* **141**, 91 – 102. (doi:10.1090/conm/141/1212579)

33. O'Malley S, Bees MA. 2012 The orientation of swimming biflagellates in shear flows. *Bull. Math. Biol.* **74**, 232 – 255. (doi:10.1007/s11538-011-9673-1)

34. Li C, Qin B, Gopinath A, Arratia P, Thomases B, Guy R. 2017 Flagellar shape data of chlamydomonas reinhardtii swimming in a Newtonian fluid and a viscocelastic fluid respectively. (doi:10.6084/m9.figshare.4879568.v7)

35. Peskin CS. 2002 The immersed boundary method. *Acta Numer.* **11**, 479 – 517.

36. Bird RB, Armstrong RC, Hassager O. 1987 *Dynamics of polymeric liquids, volume 1: fluid mechanics*. New York, NY: John Wiley & Sons.

37. Sureshkumar R, Beris AN. 1995 Effect of artificial stress diffusivity on the stability of numerical calculations and the flow dynamics of time-dependent viscoelastic flows. *J. Non-Newtonian Fluid Mech.* **60**, 53 – 80. (doi:10.1016/0377-0257(95)01377-8)

38. Thomases B. 2011 An analysis of the effect of stress diffusion on the dynamics of creeping viscoelastic flow. *J. Non-Newtonian Fluid Mech.* **166**, 1221 – 1228. (doi:10.1016/j.jnnfm.2011.07.009)

39. Howard J. 2001 *Mechanics of motor proteins and the cytoskeleton*. Sunderland, MA: Sinauer Associates.

40. Chen DT, Heymann M, Fraden S, Nicastro D, Dogic Z. 2015 ATP consumption of eukaryotic flagella measured at a single-cell level. *Biophys. J.* **109**, 2562 – 2573. (doi:10.1016/j.bpj.2015.11.003)

41. Lighthill J. 1976 Flagellar hydrodynamics. *SIAM Rev.* **18**, 161 – 230. (doi:10.1137/1018040)

42. Purcell EM. 1977 Life at low Reynolds number. *Am. J. Phys.* **45**, 3 – 11. (doi:10.1119/1.10903)

43. Gray J, Hancock GJ. 1955 The propulsion of sea-urchin spermatozoa. *J. Exp. Biol.* **32**, 802 – 814.

44. Lighthill J. 1976 Flagellar hydrodynamics. *SIAM Rev.* **18**, 161 – 230. (doi:10.1137/1018040)

45. Cox RG. 1970 The motion of long slender bodies in a viscous fluid part 1. General theory. *J. Fluid Mech.* **44**, 791 – 810. (doi:10.1017/S0022112 07000215X)

46. Tam D, Hosoi AE. 2011 Optimal feeding and swimming gaits of biflagellated organisms. *Proc. Natl Acad. Sci. USA* **108**, 1001 – 1006. (doi:10.1073/pnas.1011185108)

47. Salazar D, Roma AM, Ceniceros HD. 2016 Numerical study of an inextensible, finite swimmer in stokesian viscoelastic flow. *Phys. Fluids* **28**, 063101. (doi:10.1063/1.4953376)

48. Thomases B, Guy RD. 2017 The role of body flexibility in stroke enhancements for finite-length undulatory swimmers in viscoelastic fluids. *J. Fluid Mech.* **825**, 109 – 132. (doi:10.1017/jfm.2017.383)

49. Riley EE, Lauga E. 2014 Enhanced active swimming in viscoelastic fluids. *Europhys. Lett.* **108**, 34003. (doi:10.1209/0295-5075/108/34003)

50. Elfring GJ, Goyal G. 2016 The effect of gait on swimming in viscoelastic fluids. *J. Non-Newtonian Fluid Mech.* **234**, 8 – 14. (doi:10.1016/j.jnnfm.2016.04.005)

51. Fulford G, Blake J. 1986 Muco-ciliary transport in the lung. *J. Theor. Biol.* **121**, 381 – 402. (doi:10.1016/S0022-5193(86)80098-4)

52. Jayathilake P, Tan Z, Le D, Lee H, Khoo B. 2012 Three-dimensional numerical simulations of human pulmonary cilia in the periciliary liquid layer by the immersed boundary method. *Comput. Fluids* **67**, 130 – 137. (doi:10.1016/j.compfluid.2012.07.016)

53. Van Heel A, Hulsen M, Van den Brule B. 1998 On the selection of parameters in the FENE-P model. *J. Non-Newtonian Fluid Mech.* **75**, 253 – 271. (doi:10.1016/S0377-0257(97)00060-8)

54. Alves M, Pinho F, Oliveira P. 2001 The flow of viscoelastic fluids past a cylinder: finite-volume high-resolution methods. *J. Non-Newtonian Fluid Mech.* **97**, 207 – 232. (doi:10.1016/S0377-0257(00)00198-1)

55. Thomases B, Shelley M. 2007 Emergence of singular structures in Oldroyd-B fluids. *Phys. Fluids* **19**, 103103. (doi:10.1063/1.2783426)

56. Guy RD, Thomases B. 2015 Computational challenges for simulating strongly elastic flows in biology. In *Complex fluids in biological systems* (ed. SE Spagnolie), pp. 359 – 397. Berlin, Germany: Springer.

57. Cortez R. 2001 The method of regularized stokeslets. *SIAM J. Sci. Comput.* **23**, 1204 – 1225. (doi:10.1137/S106482750038146X)

58. Womersley R. 1999 Minimum energy (ME) interpolation points on the sphere S^2. See http://web.maths.unsw.edu.au/ rsw/sphere/images/me/me_data.html..